ALMA deep field in SSA22

Publ. Astron. Soc. Japan (2017) 69 (3), 45 (1–13)
doi: 10.1093/pasj/psx018
Advance Access Publication Date: 2017 May 4

ALMA deep field in SSA22: Blindly detected CO emitters and [C II] emitter candidates

Natsuki H. Hayatsu,[1,*] Yuichi Matsuda,[2,3] Hideki Umehata,[4,5] Naoki Yoshida,[1,6] Ian Smail,[7] A. Mark Swinbank,[7] Rob Ivison,[8] Kotaro Kohno,[5,9] Yoichi Tamura,[5] Mariko Kubo,[10] Daisuke Iono,[2,3] Bunyo Hatsukade,[2] Kouichiro Nakanishi,[2,3] Ryohei Kawabe,[2,3] Tohru Nagao,[11] Akio K. Inoue,[12] Tsutomu T. Takeuchi,[13] Minju Lee,[2,14] Yiping Ao,[2] Seiji Fujimoto,[14,15] Takuma Izumi,[5] Yuki Yamaguchi,[5] Soh Ikarashi,[16] and Toru Yamada[17,18]

[1]Department of Physics, The University of Tokyo, 7-3-1 Hongo, Bunkyo, Tokyo 113-0033, Japan
[2]National Astronomical Observatory of Japan, Osawa 2-21-1, Mitaka, Tokyo 181-8588, Japan
[3]Graduate University for Advanced Studies (SOKENDAI), Osawa 2-21-1, Mitaka, Tokyo 181-8588, Japan
[4]The Open University of Japan, 2-11 Wakaba, Mihama-ku, Chiba 261-8586, Japan
[5]Institute of Astronomy, School of Science, The University of Tokyo, 2-21-1 Osawa, Mitaka, Tokyo 181-0015, Japan
[6]Kavli Institute for the Physics and Mathematics of the Universe (WPI), Todai Institutes for Advanced Study, The University of Tokyo, 5-1-5 Kashiwanoha, Kashiwa, Chiba 277-8583, Japan
[7]Centre for Extragalactic Astronomy, Department of Physics, Durham University, South Road, Durham, DH1 3LE, UK
[8]European Southern Observatory, Karl-Schwarzschild-Str. 2, D-85748 Garching, Germany
[9]Research Center for the Early Universe, The University of Tokyo, 7-3-1 Hongo, Bunkyo, Tokyo 113-0033, Japan
[10]TMT Project Office, National Astronomical Observatory of Japan, 2-21-1 Osawa, Mitaka, Tokyo 181-8588, Japan
[11]Research Center for Space and Cosmic Evolution, Ehime University, 2-5 Bunkyo-cho, Matsuyama, Ehime 790-8577, Japan
[12]College of General Education, Osaka Sangyo University, 3-1-1 Nakagaito, Daito, Osaka 574-8530, Japan
[13]Division of Particle and Astrophysical Science, Nagoya University, Furo-cho, Chikusa-ku, Nagoya, Aichi 464-8602, Japan
[14]Department of Astronomy, Graduate School of Science, The University of Tokyo, 7-3-1 Hongo, Bunkyo, Tokyo 133-0033, Japan
[15]Institute for Cosmic Ray Research, The University of Tokyo, 5-1-5 Kashiwanoha, Kashiwa, Chiba 277-8582, Japan
[16]Kapteyn Astronomical Institute, University of Groningen, P.O. Box 800, 9700AV Groningen, the Netherlands
[17]Astronomical Institute, Tohoku University, 6-3 Aoba, Aramaki, Aoba-ku, Sendai, Miyagi 980-8578, Japan
[18]Institute of Space and Astronautical Science, JAXA, 3-1-1 Yoshinodai, Chuo-ku, Sagamihara, Kanagawa 229-8551, Japan

*E-mail: natsuki.hayatsu@utap.phys.s.u-tokyo.ac.jp

Received 2016 December 22; Accepted 2017 February 24

Abstract

We report the identification of four millimeter line-emitting galaxies with the Atacama Large Milli/submillimeter Array (ALMA) in SSA22 Field (ADF22). We analyze the ALMA 1.1-mm survey data, with an effective survey area of 5 arcmin^2, frequency ranges of 253.1–256.8 and 269.1–272.8 GHz, angular resolution of 0.″7 and rms noise of 0.8 mJy beam^{-1} at 36 km s^{-1} velocity resolution. We detect four line-emitter candidates with significance levels above 6σ. We identify one of the four sources as a CO(9–8) emitter at $z = 3.1$ in a member of the proto-cluster known in this field. Another line emitter with an optical counterpart is likely a CO(4–3) emitter at $z = 0.7$. The other two sources without any millimeter continuum or optical/near-infrared counterpart are likely to be [C II] emitter candidates at $z = 6.0$ and 6.5. The equivalent widths of the [C II] candidates are consistent with those of confirmed high-redshift [C II] emitters and candidates, and are a factor of 10 times larger than that of the CO(9–8) emitter detected in this search. The [C II] luminosity of the candidates are 4–7 $\times$ 10^8 $L_\odot$. The star formation rates (SFRs) of these sources are estimated to be 10–20 $M_\odot$ yr^{-1} if we adopt an empirical [C II] luminosity–SFR relation. One of them has a relatively low S/N ratio, but shows features characteristic of emission lines. Assuming that at least one of the two candidates is a [C II] emitter, we derive a lower limit of [C II]-based star formation rate density (SFRD) at $z \sim 6$. The resulting value of $>10^{-2}$ $M_\odot$ yr^{-1} Mpc^{-3} is consistent with the dust-uncorrected UV-based SFRD. Future millimeter/submillimeter surveys can be used to detect a number of high-redshift line emitters, with which to study the star formation history in the early universe.

Key words: early universe — galaxies: clusters: individual (SSA22) — galaxies: formation

1 Introduction

The cosmic star-formation history in the early universe has been studied in optical/near-infrared (NIR) wavelengths, which trace ultraviolet (UV) radiation in rest-frame at high redshifts (e.g., Madau & Dickinson 2014). The UV star formation rate density (SFRD) does not account for all components of star-forming galaxies (e.g., Bouwens et al. 2012, 2016). Recent studies suggest that the far-infrared (FIR) SFRD contributes more than half of the total at $z = 0$–4 (e.g., Blain et al. 1999; Barger et al. 2012; Burgarella et al. 2013; Gruppioni et al. 2013; Swinbank et al. 2014). Millimeter/submillimeter (mm/submm) galaxy surveys would, in principle, be efficient to probe the dust-obscured component of the SFRD at high-redshift (Takeuchi et al. 2005; Burgarella et al. 2013; Chen et al. 2016; Carniani et al. 2015; Fujimoto et al. 2016; Aravena et al. 2016a; Dunlop et al. 2017; Umehata et al. 2017). The advantage of such observations in mm/submm is the well-known negative k-correction; the continuum flux of a typical star-forming galaxy of fixed SFR remains approximately constant with increasing redshift (Blain et al. 2002). However, it is often difficult to estimate redshifts for very faint and dusty sources (e.g., Simpson et al. 2014).

Strong emission lines such as [C II]158 μm or [O III] 88 μm lines can be used to study the SFR and gas properties of high-z star-forming galaxies as well as to determine their spectroscopic redshifts (e.g., Colbert et al. 1999; Maiolino et al. 2005, 2015; Brauher et al. 2008; Swinbank et al. 2012; Venemans et al. 2012; De Looze et al. 2014; Inoue et al. 2014, 2016; Willott et al. 2015; Carniani et al. 2017). Interestingly, Capak et al. (2015) report that Lyman-break galaxies (LBGs) at $z = 5$–6 show enhancement of [C II] emission relative to the FIR continuum compared with mm/submm-selected galaxies. They also serendipitously detected a [C II] emitter which is faint in both the rest-UV and FIR continuum. Combining observations in rest-UV, FIR, and mm/submm emission lines appears to be essential to understanding the physical properties of galaxies at high redshifts (e.g., Bouwens et al. 2016; Aravena et al. 2016a; Dunlop et al. 2017).

One of the brightest submm emission lines is [C II] (e.g., Maiolino et al. 2005, 2009, 2015; Iono et al. 2006; Venemans et al. 2012; Swinbank et al. 2012; Willott et al. 2013, 2015; Capak et al. 2015; Díaz-Santos et al. 2016; Pentericci et al. 2016). Carbon in the interstellar medium is largely in a singly ionized state in a variety of environments, from H II regions to molecular clouds, because the ionization potential of atomic carbon is 11.3 eV, lower than that of hydrogen and close to dissociation energy of CO of 11.1 eV (e.g., Wolfire et al. 2010; Carilli & Walter 2013). The critical density of [C II]

emission is about 3×10^3 cm^{-3}, and thus [C II] emission can arise even in a molecular cloud with temperature around 92 K (Hollenbach & McKee 1989). Therefore [C II] radiative cooling often dominates in regions with a wide range of densities (e.g., Wolfire et al. 1995; Kaufman et al. 1999). Finally, [C II] emission is thought to be a potential tracer of SFR because of its main origin of a photo-dissociated region associated with young, massive stars (e.g., De Looze et al. 2011, 2014; Sargsyan et al. 2012; Kapala et al. 2015). An important observational advantage is that [C II] line emission at $z > 4$ is redshifted to wavelengths with low atmospheric absorption and thus it is possible to detect [C II] line emission even from galaxies at $z = 7$ (e.g., Venemans et al. 2012; Aravena et al. 2016b; Pentericci et al. 2016).

A number of high-redshift [C II] emitters are expected to be detected during forthcoming high-sensitivity observations with the Atacama Large Millimeter/submillimeter Array (ALMA) (e.g., Geach & Papadopoulos 2012; da Cunha et al. 2013; Matsuda et al. 2015; Aravena et al. 2016b). In this paper, we present a blind search for [C II] emitters using ALMA Cycle 2 data (Umehata et al. 2017). We briefly introduce the observations in section 2. The details of our data analysis is described in section 3. Then we show the results in section 4 and discuss the implications for cosmic star formation history in section 5. We summarize the results and discussions in section 6. Throughout the paper, we adopt the standard ΛCDM cosmology with the matter density $\Omega_{\rm M} = 0.3$, the cosmological constant $\Omega_\Lambda = 0.7$, and the Hubble constant $h = 0.7$ in the unit of $H_0 = 100\,h\,{\rm km\,s^{-1}\,Mpc^{-1}}$. All magnitudes are given in the AB system, unless otherwise noted. We calculate SFR assuming the Chabrier initial mass function (IMF) (Chabrier 2003), with an integration range of from $0.08\,M_\odot$ to $100\,M_\odot$. When needed, we use the conversion factor of 1.8 from the Chabrier IMF to the equivalent Salpeter IMF (Salpeter 1955) and 1.1 from the Chabrier IMF to the Kroupa IMF (Kroupa 2001).

2 Observation

We analyze data from the ALMA Deep Field survey of SSA22 (ADF22) observed in Band 6 in ALMA Cycle 2 in 2014 June and 2015 April (Proposal ID 2013.1.00162.S, PI: H. Umehata). The details of the observation are described in Umehata et al. (2017).

ADF22 is a survey field with an area of $2' \times 3'$ centered on a $z = 3.09$ proto-cluster; RA (J2000.0) = $22^{\rm h}17^{\rm m}34^{\rm s}$, Dec (J2000.0) = $+00^\circ17'00''$ consisting of 103 pointing fields. The field was observed using four 1.875-GHz spectral windows (SPWs) with the central frequency of 263 GHz, which corresponds to the [C II] redshift of $z = 6.2$.

The typical angular resolution of combined data is $0''.72 \times 0''.62$ corresponding to $\sim$6 kpc at $z = 6.2$. The on-source time per pointing in the fields is 4.5 min. The data observed in 2014 and 2015 have angular resolutions of $0''.54 \times 0''.49$ and $1''.24 \times 0''.87$, and on-source times per pointing in the fields of 2.5 min (for 2014) and 2.0 min (for 2015).

The four SPWs have root-mean-square (rms) noise levels of 0.7, 0.7, 0.8, and 0.9 mJy beam^{-1} at a 36 km s^{-1} velocity resolution. The rms values of each SPW at 36 km s^{-1} resolution of combined, 2014, and 2015 data as a function of the observed frequency are shown in figure 1, where no significant atmosphere absorption is seen. Other properties of the data are listed in table 1.

In order to search faint emission-line sources, we use high-sensitivity data of 80 pointing fields, Field 1–Field 80, and search in a rectangle area of $\sim$5 arcmin^2; [RA (J2000.0), Dec (J2000.0)] = ($22^{\rm h}17^{\rm m}31^{\rm s}.86$, $+00^\circ15'25''.46$) to ($22^{\rm h}17^{\rm m}38^{\rm s}.17$, $+00^\circ18'35''.05$), and a frequency coverage

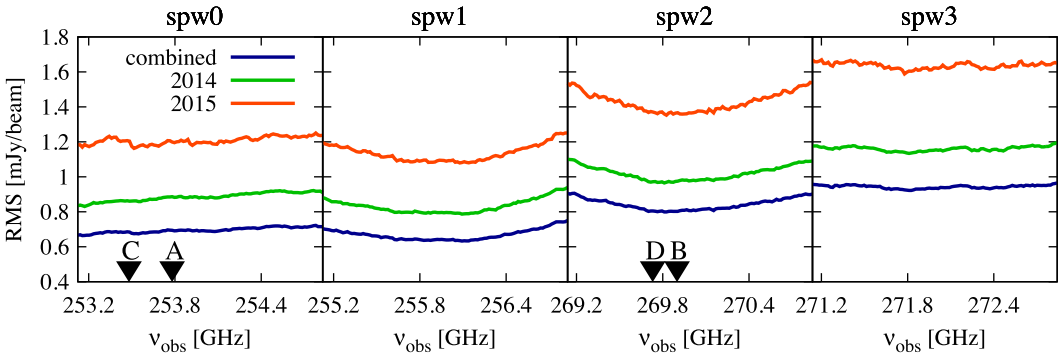

Fig. 1. The rms noise level of the four spectral windows (SPWs) analyzed in this work at velocity resolution 36 km s^{-1} as a function of observed frequency. In each panel, we plot the rms of combined data and the individual data obtained in 2014 and in 2015. We also mark the frequencies of the detected four line-emitter candidates A–D. Typical rms values are also given in table 1. We note that the data observed in 2014 and 2015 have different angular resolutions. (Color online)

Table 1. Properties of the datacube of four spectral windows.*

SPW ID	ν_{obs}* [GHz]	$z_{[CII]}$†	dv‡ [km s^{-1}]	Angular resolution§ [']	rms of original data‖ [mJy beam^{-1}]	# of net clumps♯	# of matched clumps	Max. positive S/N ratio	Max. negative S/N ratio
0	253.12–254.83	6.458–6.508	18.3	0.67, 0.53, 1.09	0.7, 0.9, 1.2	25/18	9/10	7.77σ (10)**	5.70σ (2)
1	255.14–256.83	6.400–6.449	18.1	0.68, 0.54, 1.11	0.7, 0.8, 1.1	6/4	5/3	5.73σ (6)	5.81σ (0)
2	269.14–270.84	6.017–6.062	17.2	0.62, 0.49, 1.02	0.8, 1.0, 1.4	18/14	7/6	6.51σ (21)	6.05σ (6)
3	271.14–272.84	5.966–6.009	17.1	0.62, 0.49, 1.01	0.9, 1.2, 1.6	10/21	5/10	5.99σ (21)	6.30σ (8)

*Observed frequency range we use for the search.
†[C II] redshift range corresponding to the observed frequency range.
‡Mean velocity corresponding to an interval of slices.
§Mean angular resolution. Column shows combined data, 2014 data, and 2015 data.
‖1σ sensitivity at 36 km s^{-1} spectral resolution calculated by using primary beam corrected data. This column is set in the same manner as the "Angular resolution" column.
♯Number of clumps detected by CLUMPFIND (Williams et al. 1994) in original/inverted S/N cubes.
**Numbers in bracket represent the size of slices smoothed in the spectral domain of the S/N cube.

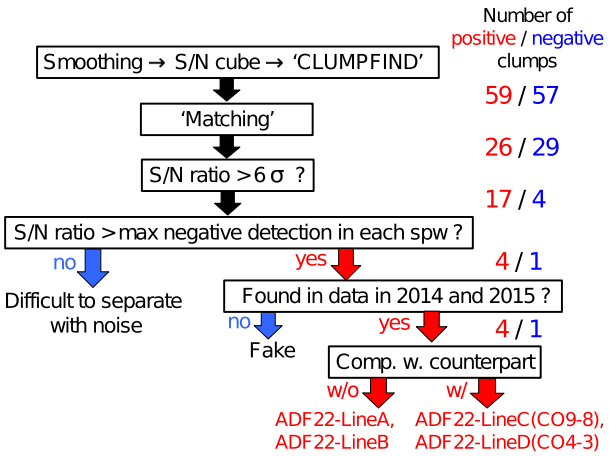

Fig. 2. Flowchart of our selection method. The number of retained clumps with >5.5σ at each step is given on the right. We select the targets by setting a S/N threshold 6.0σ in each SPW, and then by imposing that their S/N ratios are larger than the maximum negative S/N ratio (see also table 1). Finally, the selection leaves four clumps as line emitting galaxy candidates. (Color online)

of 253.1–272.8 GHz (table 1). The effective survey area corresponds to about 29 (comoving) Mpc^2 and the effective survey volume is $\sim 2.2 \times 10^3$ (comoving) Mpc^3 at $z = 6.2$.

3 Method

The flowchart of our source selection method is shown in figure 2. The data are analyzed with Common Astronomy Software Application (CASA) ver. 4.5.3 (McMullin et al. 2007). We make a continuum-subtracted datacube by using UVCONTSUB and CLEAN. We first spectrally smooth the data to obtain high signal-to-noise (S/N) ratios. The top-hat spectral smoothing window is set to be 0, 2, 4, ..., 12, 15, 18, ..., 21 slices, with a slice width corresponding to $\sim$18 km s^{-1}. We use the spectral smoothing function "boxcar" so that the velocity sampling of the output data is kept constant. As each spectral data slice has a different rms value, as shown in figure 1, we normalize each slice by its rms. We call a thus-generated datacube an "S/N cube".

We use CLUMPFIND (Williams et al. 1994) to search emission line sources in the S/N cube. We search for sources with a "low" CLUMPFIND threshold value of $\geq$4.5. We then perform "matching" of the clumps detected at the same position between the S/N cubes in the same SPW with different resolutions and retain the clump that has the maximum S/N ratio (see also table 1). We select clumps that have an S/N ratio larger than 6.0σ and also larger than the maximum negative S/N ratio measured in the inverted S/N cube in each SPW (see also figure 2), in order to avoid contamination by spurious sources (e.g., Hatsukade et al. 2016). We also check line spectral features of the detected clumps (sources) in the datacube separately for those observed in 2014 and 2015.

For the detected sources, we search for counterparts of the detected clumps from data in the u^* band observed by the Canada France Hawaii Telescope/MegaCam and obtained from archival data (Kousai 2011), in the B, V, R, i', z', *NB912*, J, H, and K bands observed by the Subaru Telescope (Hayashino et al. 2004; Nakamura et al. 2011; Suzuki et al. 2008; Uchimoto et al. 2012), in the 3.6 μm, 4.5 μm, 5.8 μm, 8.0 μm, and 24 μm taken with the Spitzer Space Telescope/IRAC and MIPS (Hainline et al. 2009; Webb et al. 2009), and in the 0.5 keV, 2 keV, and 8 keV taken with the Chandra X-Ray Observatory (Lehmer et al. 2009).

[C II] line emitting galaxies at $z = 6.0$–6.5 are likely to be detected only longward of the z' band and/or in the narrow-band *NB912* if they are LBGs or Lyα emitters (LAEs) (e.g., Nakamura et al. 2011), although the available z'-band and *NB912* data could be too shallow for high-redshift [C II] emitters in our blind search. For the sources with counterparts, we estimate either their photometric redshift by means of spectral energy distribution (SED) fitting or spectroscopic redshift by assuming their line species. SED

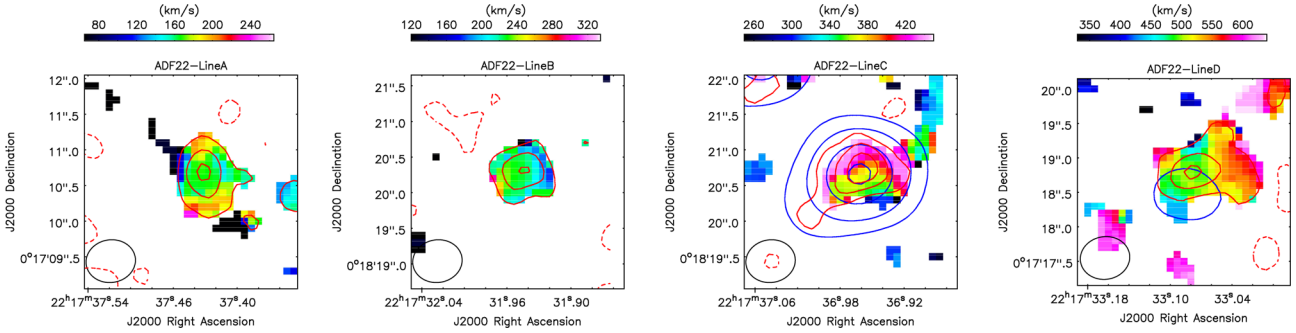

Fig. 3. We plot the continuum-subtracted first moment maps of the four candidates. The images are made by using the spectrally smoothed data. The colormaps show the projected velocity field with $>2\sigma$ around each target. The velocity is measured with respect to the center of each SPW. The red contours denote -2σ, 2σ, 4σ, and 6σ, with negative contours shown by dashed lines, whereas the blue contours show the S/N ratio of the continuum, with 4σ, 10σ, 20σ, 30σ. ADF22-LineA and LineB are not detected in the 1.1-mm continuum. The beam size is shown at the bottom left-hand corner of each panel. (Color online)

fitting is calculated by using HYPERZ software (Bolzonella et al. 2000). In subsection 4.3, we also use the equivalent width and the source number density to consider if the detected [C II] emitter candidates are other line emitters.

4 Result

4.1 Source detection

We detect four line-emitter candidates. Hereafter, we call the two sources without optical, NIR, or FIR counterparts "ADF22-LineA" and "ADF22-LineB". Those with counterparts are dubbed "ADF-LineC" and "ADF-LineD". The peak S/N ratios are 6.5σ, 6.2σ, 7.7σ, and 6.5σ, for ADF22-LineA, B, C, and D, respectively. The first moment images of the candidates are shown in figure 3, and their properties are shown in table 2.

Figure 4 shows the cumulative number of positive and negative clumps as a function of S/N ratio. Although the S/N ratios of ADF22-LineA, B, and D are below 6σ at the original spectral sampling, the lines are detected at $\geq 6\sigma$ in the smoothed S/N cubes. We compare the spectral line features of the emitter candidates in different observation epochs, 2014 and 2015 (figure 5). Overall, the contiguous positive signals over a velocity range of $\geq 180\,\mathrm{km\,s^{-1}}$ and the line features commonly seen suggest that the candidates are likely real sources.

We note here that we also detect one clump with 6.3σ in the inverted S/N cube, and thus we would naively be concerned that one candidate with 6.2σ could be a spurious source. However, the most-negative clump is actually detected in SPW 3, where none of our four candidates are located. We also find that a datacube with a higher rms value has a higher maximum negative detection, and that SPW 3 is the data with the lowest sensitivity (table 1). Since the datacubes in different SPWs have different properties, the existence of the high-σ negative clump in SPW 3 does not immediately impact the confidence of our line-emitter candidates. ADF22-LineB has a lower S/N ratio than ADF22-LineA, whereas it has non-negative z'-band counterparts with $<3\sigma$ (see also figure 6). Velocity-gradient is also seen around ADF22-LineB (see also figure 3).

4.2 Line identification

Figure 6 shows the images of the four candidates in B, V, z', 3.6-μm, and 1.1-mm wavebands. We plot the SED and model fit for ADF22-LineD in figure 7, and the measured photometry in the detected bands are given in table 3. The photometric redshift is estimated by using HYPERZ (Bolzonella et al. 2000). We fit the SED templates to the spectral coverage from UV to 8 μm by following Bruzual and Charlot (1993), assuming a Calzetti dust extinction law (Calzetti et al. 2000). We also use SED templates from the SWIRE library (Polletta et al. 2007).

ADF22-LineA and B: We do not find any secure counterpart nor close sources within 2″ of the sources. Therefore we regard LineA and LineB as good [C II] emitter candidates.

ADF22-LineC: LineC very likely arises from the galaxy ADF22.4 reported in Umehata et al. (2017), the redshift of which is determined to be $z = 3.091$ from FIR spectroscopic follow-up observations (H. Umehata et al. in preparation). Thus we identify ADF22-LineC as CO(9–8) line emission at $z = 3.091$. In addition, the optical component near ADF22-LineC is a known galaxy at $z = 0.55$ (Kubo et al. 2015), but we exclude the possibility of ADF22-LineC being at $z = 0.55$ because there is no obvious line species observed at 1.1 mm. LineC is also detected in X-ray (Lehmer et al. 2009), which may indicate that ADF22-LineC is an AGN-host galaxy. Further details of this galaxy will be discussed in H. Umehata et al. (in preparation).

Table 2. Measured and derived candidate properties.*

ADF22 ID	Name (J2000.0)	$\nu_{\rm peak}$ [GHz]	$S_{\rm peak}/N$* [σ]	Smoothing† [km s^{-1}]	$S_{1.1{\rm mm}}$‡ [mJy]	$S_{\rm line}$§ [Jy km s^{-1}]	FWHM‖ [km s^{-1}]	$EW_{\rm obs}$ [μm]	z#	$\log_{10}L_{\rm line}$** [$L_\odot$]	$\log_{10}L_{\rm FIR}$†† [$L_\odot$]
ADF22-LineA	ALMA J221737.43+001710.7	253.79	6.5	220 (12)	<0.2	0.4 ± 0.1	220 ± 40	>8.6	6.489	$8.6^{+0.2}_{-0.2}$	<11.4
ADF22-LineB	ALMA J221731.95+001820.3	269.92	6.2	258 (15)	<0.2	0.7 ± 0.1	220 ± 45	>14.6	6.041	$8.8^{+0.2}_{-0.3}$	<11.4
ADF22-LineC	ALMA J221736.97+001820.8	253.49	7.8	220 (12)	2.0 ± 0.1	0.5 ± 0.1	140 ± 20	$1.1^{+0.2}_{-0.2}$	3.091	$8.0^{+0.2}_{-0.2}$	$12.6^{+0.2}_{-0.1}$
ADF22-LineD	ALMA J221733.07+001718.8	269.70	6.5	361 (21)	0.7 ± 0.2	1.0 ± 0.1	240 ± 40	7.3^{+5}_{-2}	0.709	$6.7^{+0.2}_{-0.3}$	$11.9^{+0.2}_{-0.2}$

*Maximum S/N ratio of the clump in all S/N cubes.
†Smoothing window of the datacube with maximum positive S/N ratio. Numbers in brackets represent the corresponding size of slices.
‡3σ upper limit is estimated in Umehata et al. (2017).
§Integrated line flux estimated by IMFIT.
‖Full-width at half-maximum derived by Gaussian fit.
#The redshift derived from $\nu_{\rm peak}$. The uncertainty is $O(10^{-3})$.
**Line emission of [C II] 1900.543 GHz, [C II], CO(9–8) 1036.912 GHz, and CO(4–3) 461.041 GHz.
††We estimate the $L_{\rm FIR}$ of ADF22-LineA, B, and D by usingthe SED fitting method of Chary and Elbaz (2001). $L_{\rm FIR}$ of ADF22-LineC is referred to estimation of Umehata et al. (2017).

ADF22-LineD: LineD is spatially consistent with the position of the tentatively detected continuum source ADF22.21 reported in Umehata et al. (2017). The result of SED fitting shows that reduced χ^2 values reach a minimum at $z\sim0.6$–0.8 (figure 7, left-hand panel). Interestingly, the SED is well fitted by that of Arp220 placed at $z\sim0.7$ (figure 7, right-hand panel). By searching for possible lines in this redshift range, we conclude that ADF22-LineD is likely a CO(4–3) emitter at $z=0.71$.

4.3 Possibility of other line emissions

Besides the [C II] line emission, there are also possibilities that ADF22-LineA and LineB are other emission line sources, such as ^{12}CO line emission at $z\leq3.1$, H_2O at $z\sim1.9$ or 2.8, [N II]205 μm at $z\sim4.6$, [O I]145 μm at $z\sim6.9$, [N II]122 μm at $z\sim8.5$, or [O III]88 μm at $z\sim12$ (Swinbank et al. 2012; Tamura et al. 2014; Ono et al. 2014; Decarli et al. 2016a; Aravena et al. 2016b).

If ADF22-LineA and LineB are ^{12}CO emitters, the number density is consistent with the result of the ALMA Spectroscopic Survey (ASPECS) by Decarli et al. (2016a) and with semi-analytical/empirical predictions referred to their references therein (Lagos et al. 2012; Popping et al. 2016; Vallini et al. 2016). Thus we cannot exclude the possibility of ^{12}CO emitters by the discussion of detectability.

We compare the equivalent widths (EWs) in the observed frame of the four candidates. The estimated EWs are >8.6, >14.6, 1.1, and 7.3 μm for ADF22-LineA, B, C, and D, respectively, assuming a 3σ continuum flux limit. ADF22-LineA and B have higher EW than the blindly detected^{12}CO emitters in our survey. The left-hand and middle panels of figure 8 also show the distribution of the EWs in the 0.9–1.3 mm observed frame of the four candidates, high-redshift [C II] emitting LBGs and LAEs (Capak et al. 2015; Pentericci et al. 2016), [C II] emitter candidates detected in ASPECS (Aravena et al. 2016b), and ^{12}CO emitter candidates detected in band 6 in ASPECS (Decarli et al. 2016b). The EWs of ADF22-LineA, B, and other high-redshift [C II] emitter/candidates are comparable. Given this information, we argue that ADF22-LineA and B are more likely to be [C II] emitters at $z=6.5$ and 6.0 than CO emitters at $z\leq3.1$. EW values of ADF22-LineA and B are comparable to those of the blindly detected CO emitters. Further consideration by using forthcoming follow-up observation and theoretical study will be needed to yield any insight into the trends of EW distributions. As with ADF22-LineA and B, blindly detected line-emitter candidates are expected often to have no counterpart (Aravena et al. 2016b). Thus it is important to study the EWs of a large sample of CO/[C II] emitters. We note that H_2O molecular lines are expected to

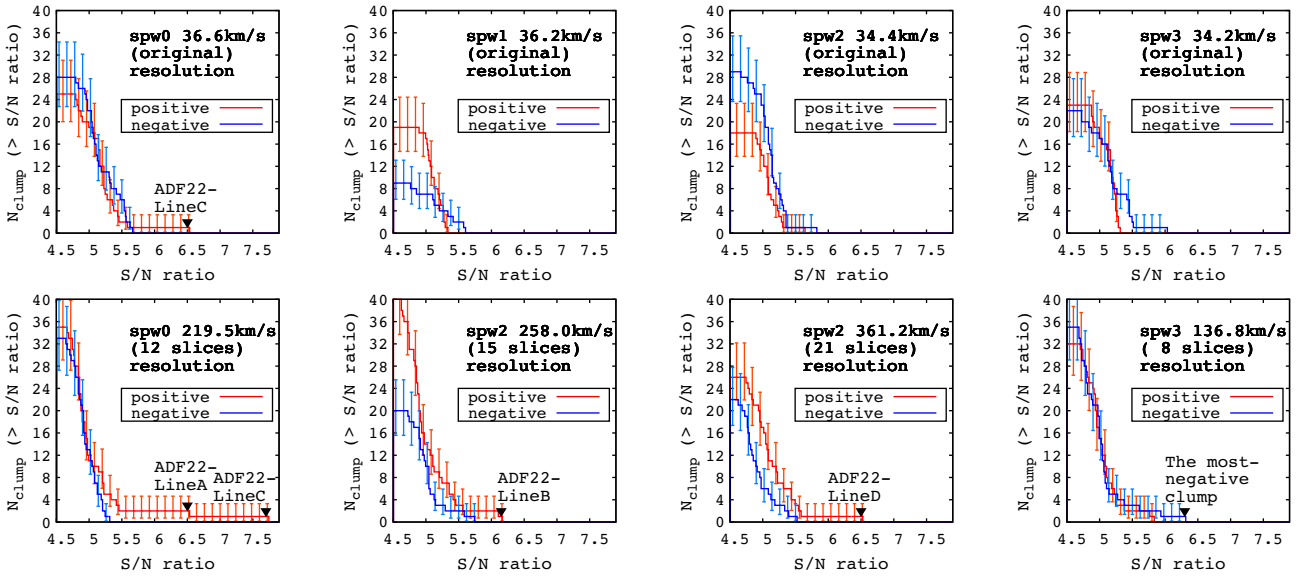

Fig. 4. Cumulative number of positive and negative clumps as a function of S/N, with 1σ error bars from the source number statistics (Gehrels 1986). We use the continuum-subtracted S/N cubes before "matching". The top panels show the number distributions with our fiducial spectral resolution. ADF22-LineC is detected with 6.5σ in the S/N cube at the fiducial resolution. The bottom panels show the result with smoothed spectral resolutions. ADF22-LineA and ADF22-LineC are detected in the S/N cube at 220 km s^{-1} spectral smoothing, ADF22-LineB at 258 km s^{-1} spectral smoothing, and ADF22-LineD at 361 km s^{-1} spectral smoothing. ADF22-LineD is also detected with 6.1σ at 258 km s^{-1} spectral smoothing. The most-negative clump detected in SPW 3 has an S/N ratio of 6.3σ in the inverted S/N cube. (Color online)

have similar line fluxes to CO line emission in the submm band (e.g., Rangwala et al. 2011; Omont et al. 2013), and thus can be distinguished from high-redshift [C II] emitters by comparing their EWs.

The [C II] luminosity, $L_{[\mathrm{C\,II}]}$, of ADF22-LineA and B is calculated by using the luminosity distance D_{L}, the observed frequency ν_{o}, and the velocity-integrated flux S^{v} (e.g., Carilli & Walter 2013):

$$\frac{L_{[\mathrm{C\,II}]}}{L_{\odot}} = 1.04 \times 10^{-3} \left(\frac{D_L}{\mathrm{Mpc}}\right)^2 \frac{\nu_{\mathrm{o}}}{\mathrm{GHz}} \frac{S^{\mathrm{v}}}{\mathrm{Jy\,km\,s^{-1}}}. \quad (1)$$

The estimated $L_{[\mathrm{C\,II}]}$ of 4–7 $\times 10^8\,L_{\odot}$ is consistent with the values of normal star-forming galaxies in the local universe (e.g., Swinbank et al. 2012), thus we do not consider the effect of a [C II] line deficit (e.g., Graciá-Carpio et al. 2011; Díaz-Santos et al. 2013). We then derive the [C II] luminosity function by using the SFR–[C II] luminosity relation (De Looze et al. 2014) and the SFR function at $z = 6$ (Smit et al. 2012). The right-hand panel of figure 8 shows that the detection of one [C II] emitter candidate in the survey area is roughly consistent with the expected [C II] number counts, if we use the SFR–$L_{[\mathrm{C\,II}]}$ relation from De Looze et al. (2014) that is calibrated from observations of nearby low-metallicity dwarf galaxies (see also section 5):

$$\frac{SFR_{[\mathrm{C\,II}]}}{M_{\odot}\mathrm{yr}^{-1}} = 10^{-5.73\pm0.32} \left(\frac{L_{[\mathrm{C\,II}]}}{L_{\odot}}\right)^{0.80\pm0.05}. \quad (2)$$

We also plot the predicted number counts of [N II] 122 μm and [N II] 205 μm from the model of Orsi et al. (2014). The predicted number count of [O III] 88-μm emission at $z \sim 12$ is lower than the [N II] 122-μm emission (Orsi et al. 2014). It is expected that such line emitters will not be found in our survey area. From the discussion above, we assume ADF22-LineA and B to be [C II] emitter candidates.

5 Discussion

In order to discuss the cosmic star formation history, we derive the SFRs of ADF22-LineA and ADF22-LineB assuming that they are [C II] emitters at $z = 6$. We calculate the total SFR by summing up the dust-uncorrected $\mathrm{SFR_{UV}}$ and $\mathrm{SFR_{IR}}$, resulting in $\mathrm{SFR_{UV+IR}}$ (e.g., Buat et al. 2010), by using the following equations (Kennicutt 1998):

$$\frac{SFR_{\mathrm{UV}}}{M_{\odot}\,\mathrm{yr}^{-1}} = 7.8 \times 10^{-29} \frac{L_{\nu}}{\mathrm{erg\,s^{-1}\,Hz^{-1}}}, \quad (3)$$

$$\frac{SFR_{\mathrm{IR}}}{M_{\odot}\,\mathrm{yr}^{-1}} = 2.5 \times 10^{-44} \frac{L_{\mathrm{IR}}}{\mathrm{erg\,s^{-1}}}, \quad (4)$$

where L_{ν} refers to the UV luminosity density in the wavelength range 1500–2800 Å, and L_{IR} refers to the IR luminosity integrated over 8–1000 μm. We estimate the L_{IR} of ADF22-LineA, B, and D from the observed 1.1-mm continuum fluxes by using the SED fitting method of Chary and

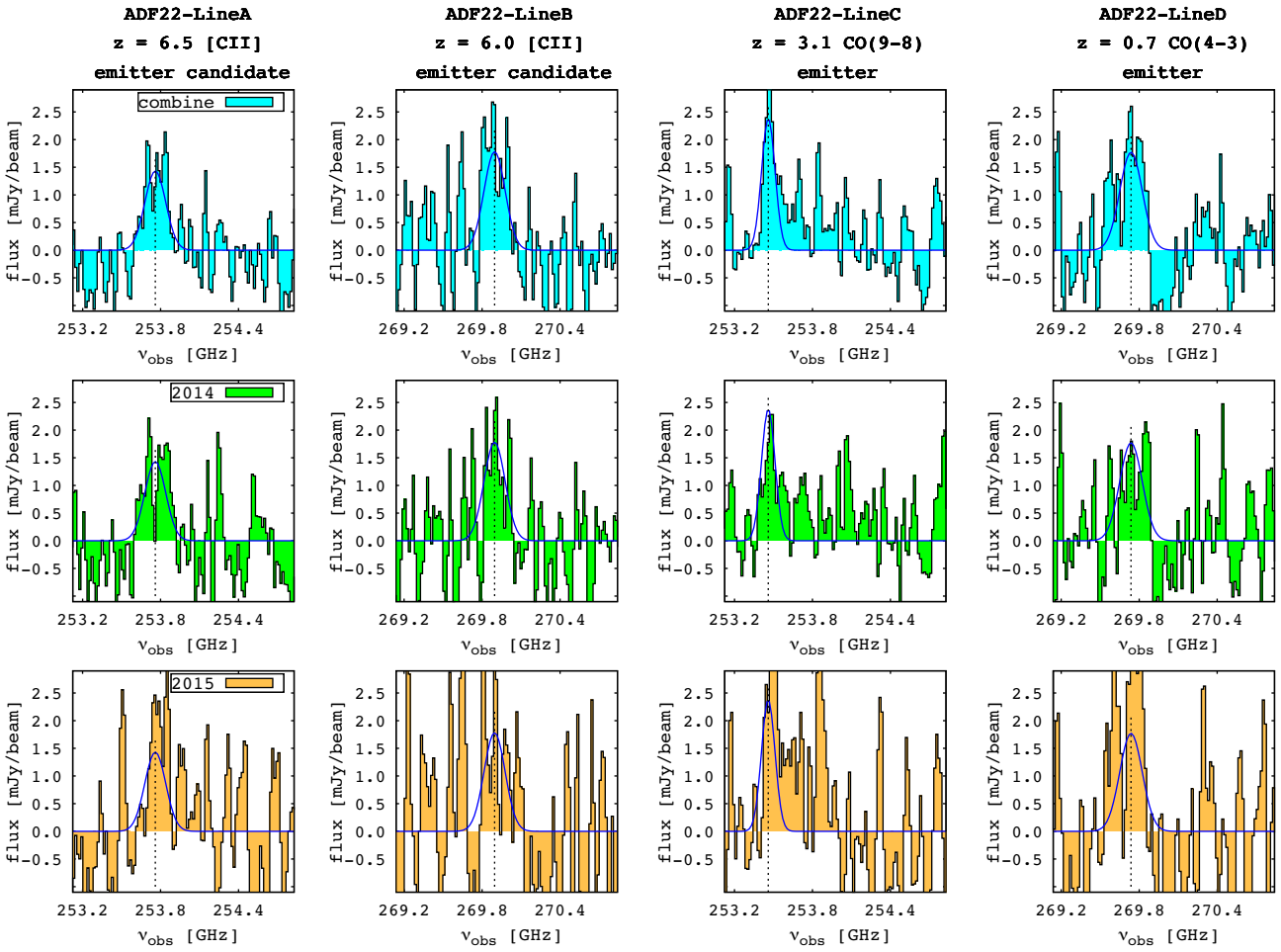

Fig. 5. Spectra of our four line-emitter candidates. We use continuum-subtracted image data in original spectral resolution. The top panels show the combined data observed in 2014 and 2015, whereas the middle and the bottom panels show separately the data observed in 2014 (green) and the data observed in 2015 (orange). The blue curve in each panel shows the best-fitting Gaussian profile for the combined data. ADF22-LineA and LineB are the candidate [C II] emitters from our survey. (Color online)

Elbaz (2001). Continuum upper limits of ADF22-LineA and B are assumed to be 3σ. The $L_{\rm IR}$ of ADF22-LineC is referred to estimation calculated by Umehata et al. (2017). The upper limit of the UV luminosity is estimated in Nakamura et al. (2011). The obtained $\mathrm{SFR_{UV+FIR}}$ is $<30\,M_\odot\,\mathrm{yr}^{-1}$, being consistent with the SFR–$L_{\rm [C\,II]}$ relation of De Looze et al. (2014) that is calibrated by local low-metallicity dwarf galaxies (figure 8, left-hand panel). We note that the relation calibrated by high-z galaxies is considered to be applicable to bright [C II] emitters with $>10^9\,L_\odot$ (De Looze et al. 2014) and exceeds the $\mathrm{SFR_{UV+FIR}}$ upper limit for the candidates in this survey. The estimated $\mathrm{SFR_{[C\,II]}}$ values from the low-metal dwarf relation are $13^{+4}_{-5}\,M_\odot\,\mathrm{yr}^{-1}$ for ADF22-LineA and $20^{+9}_{-10}\,M_\odot\,\mathrm{yr}^{-1}$ for ADF22LineB (see also table 3).

We estimate the [C II] luminosity function (LF) at $z\sim6.2$ from only one source, because one of the two [C II] candidates has a relatively low σ and thus could possibly be a spurious source (see subsection 4.1). We show this result in figure 9 and compare it to [C II] LFs from previous studies. The estimated [C II] LFs at $z=0.0$ (Swinbank et al. 2012; Hemmati et al. 2017) are derived from the follow-up observation of the IRAS sources (Brauher et al. 2008) or samples from the Great Observatories All-sky LIRG Survey (Díaz-Santos et al. 2013). We indicate the upper limit at $z=4.4$ derived by Matsuda et al. (2015) using ALMA Cycle 0 archive data, and the lower limit at $z=4.4$ based on two serendipitous detections in the ALMA LABOCA ECDFS Submillimeter Survey (ALESS: Swinbank et al. 2012). The estimation at $z=5$–6 is derived from a follow-up observation by Capak et al. (2015). We also indicate the estimation of an over-dense region at $z=6$ by Miller et al. (2016). The constraint for [C II] LF at $z=6$–8 is provided by the result of ASPECS (Aravena et al. 2016b), which is based on an assumption that all [C II] candidates are real [C II] emitters. As discussed in subsection 4.2, we also derive a simple model of the [C II] luminosity function at $z=6$ by using the SFR–$L_{\rm [C\,II]}$ relation

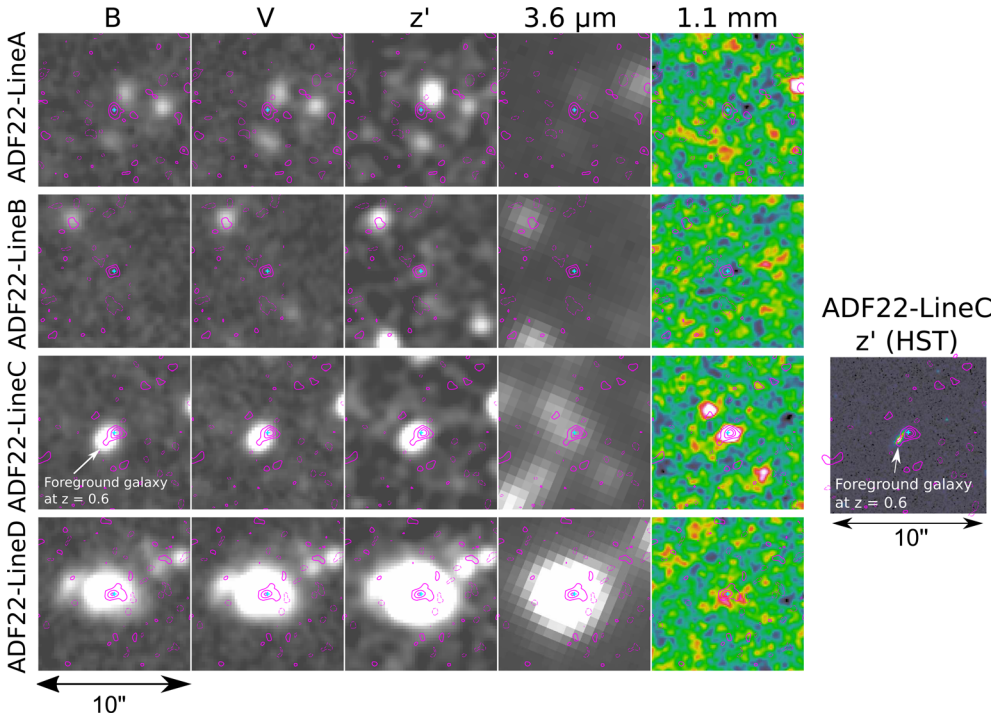

Fig. 6. Images of the four line-emitter candidates at different wavelength range from optical to 1.1 mm. In each panel, the cyan cross indicates the position of the candidate. The magenta contours show the 0th moment images of the line emission with 2σ, 4σ, and 6σ, and the dashed contours show that with -4σ and -2σ. We adopt a linear colour-scale for this figure. Counterparts are not found at the position of LineA or LineB at any wavelength. We also show a z'-band image of LineC taken by HST Advanced Camera for Surveys I (*F814W*)-band in archive (PID 9760) in the rightmost panel. (Color online)

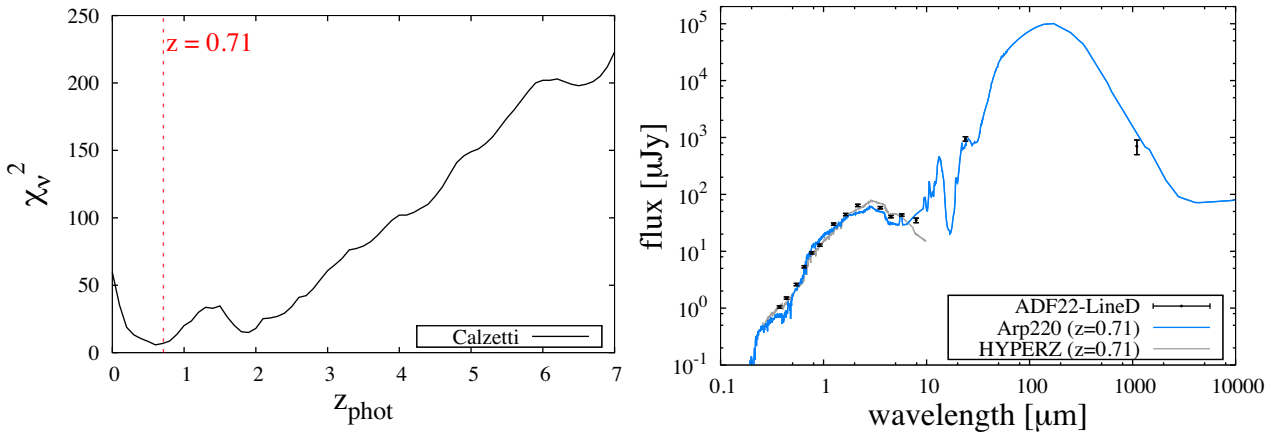

Fig. 7. Left: Estimated reduced χ^2 as a function of photometric redshift for the ADF22-LineD (right). The χ_ν^2 value becomes minimum at $z = 0.6$–0.8. Right: SEDof ADF22-LineD (right). The SED is well fitted by that of Arp220 placed at $z \sim 0.71$. (Color online)

(De Looze et al. 2014) and the SFR function at $z = 6$ (Smit et al. 2012). Our [C II] LF model is close to our own observational result and results of the other studies, whereas the estimated LFs based on the empirical relations for high-redshift, and for all galaxies (De Looze et al. 2014), do not match the observational result at $z > 4$. We note that if the completeness of the detection is lower than unity, the estimated [C II] LF represents the lower limit.

We calculate a conservative limit of [C II] SFRD from the mean of the $SFR_{[C\,II]}$ of the two sources divided by the survey volume (figure 10). The derived [C II] SFRD is $>7.5 \times 10^{-3}\,M_\odot\,yr^{-1}\,Mpc^{-3}$. Interestingly, this is close to the dust-uncorrected UV SFRD at $z = 6.2$. The input of the only [C II] emitter with faint UV and dust emission to the cosmic SFRD might already constitute a major contribution. The result may imply the existence of an untraceable

Table 3. Photometry.[†]

ADF22 ID	u^*	B	V	R	i'	z'	J
ADF22-LineA,B	>26.6	>27.0	>27.1	>27.2	>26.9	>26.2	>24.2
ADF22-LineD	23.84 ± 0.05	23.46 ± 0.03	22.86 ± 0.01	22.08 ± 0.01	21.47 ± 0.01	21.13 ± 0.01	19.79 ± 0.01
ADF22 ID	H	K_s	3.6 μm	4.5 μm	5.8 μm	8.0 μm	24 μm
ADF22-LineA,B	>24.1	>24.1	>24.9	>24.1	>22.0	>21.6	>28.0
ADF22-LineD	20.21 ± 0.02	19.39 ± 0.01	19.49 ± 0.01	19.88 ± 0.02	19.81 ± 0.05	20.04 ± 0.10	16.46 ± 0.10

[†]All units of photometry flux is AB magnitude. Upper limits are given by 3σ. We use the data taken with CFHT MegaCam u^* (in the archive, P.I. Cowie, see also Matsuda et al. 2004), Subaru Suprime-Cam B, V, R, i', z' bands (Matsuda et al. 2004), Subaru MOIRCS J, H, K_s (Uchimoto et al. 2012) and the Spitzer IRAC 3.6-, 4.5-, 5.8-, and 8.0-μm (Webb et al. 2009) band photometry. The PSF differences in $u^* \sim 8.0\,\mu$m are corrected following Kubo et al. (2013). The 24-μm photometry flux is calculated over a 2″ diameter aperture.

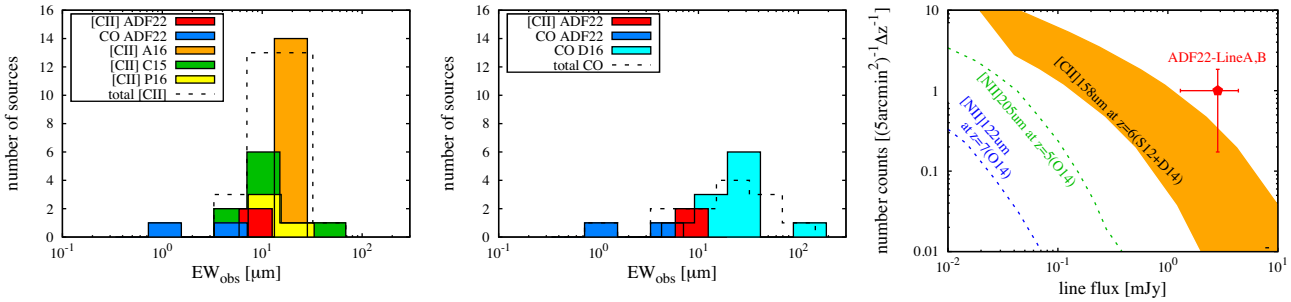

Fig. 8. Left and middle: We compare the distribution of EWs in the 0.9–1.3 mm observed frame—the ADF22 sources with high-redshift [C II] emitters/candidates (left) and low-redshift CO emitters/candidates (middle) (Capak et al. 2015; Aravena et al. 2016b; Pentericci et al. 2016; Decarli et al. 2016b). The continuum upper limit is assumed to be 3σ. The histograms except for the case of ADF22 CO emitters contain the data with lower limits. EW values of ADF22 [C II] emitter candidates are comparable to other high-redshift [C II] emitters/candidates and ADF22 CO emitters have at most a factor of 10 times lower values. For CO emitters, their transitions are from $j = 9$–8 to 3–2, which are not corrected to a fixed transition. ADF22 [C II] emitter candidates are consistent with the CO distribution, using observational data available. Right: Cumulative number counts of [N II]-, and [C II]-line emitters, where Δz is set to be the survey redshift range. The red point represents the number density of this survey for one [C II] emitter candidate with a 1σ error bar from the source number statistics (Gehrels 1986). The orange region shows the [C II] emitter number count estimated (converted) from the star formation rate function at $z = 6$ (Smit et al. 2012) and the SFR–$L_{[C\,II]}$ relation (De Looze et al. 2014). The velocity width is assumed to be 200 km s^{-1}. This simple model shows agreement to the observed number count. The dotted lines show [N II]-emitter number counts from Orsi et al. (2014), which are well below the observational result. We also note that the [O III] number counts at $z \sim 12$ are below the [N II]122 μm counts (Orsi et al. 2014). (Color online)

component of the SFRD observed by rest-UV. In order to confirm the truth of this, the estimation of a faint-end slope of the [C II] LF would be crucial.

In figure 10, we also derive upper limits of SFRDs at $z = 7$–12 from the non-detections of [O I] 145-μm, [N II] 122-μm, and [O III] 88-μm lines in our search, as discussed in subsection 4.3. The SFRs are calculated from line luminosities by using observational relations estimated by Farrah et al. (2013). This result demonstrates that line surveys enable us to estimate SFRDs at multiple redshifts at once.

There are a few possible mechanisms for the [C II] line emission to be particularly intense relative to FIR and UV emission. For example, it can be caused by high far-UV radiation from massive, young stars in the early universe (e.g., Wolfire et al. 1995). The environment of a low-metallicity and a low dust-to-gas ratio can also cause enhancement of [C II] radiative cooling (Wolfire et al. 1995; Capak et al. 2015). In particular, the low dust-to-metal environment may not only enhance [C II] line emission but also weaken dust continuum emission (Inoue 2003; Asano et al. 2014). Hot dust dominates the short-wavelength portion of the SED (Casey et al. 2014; Zhou et al. 2016), making the dust continuum at long wavelengths relatively suppressed. The size distribution of dust grains also affect faint FIR continuum (Takeuchi et al. 2003, 2005). Altogether, observations in the submm band can provide invaluable information on the physical properties of high-redshift galaxies. Future deep submm surveys will enable us to understand the formation of galaxies and to probe the early cosmic star-formation history.

6 Summary

We search millimeter line emitters by using 1.1-mm ADF22 survey data taken in ALMA Cycle2. Our newly constructed method for line searches worked for detecting two CO emitters at $z = 0.7$ and 3.1 and two [C II] emitter candidates at

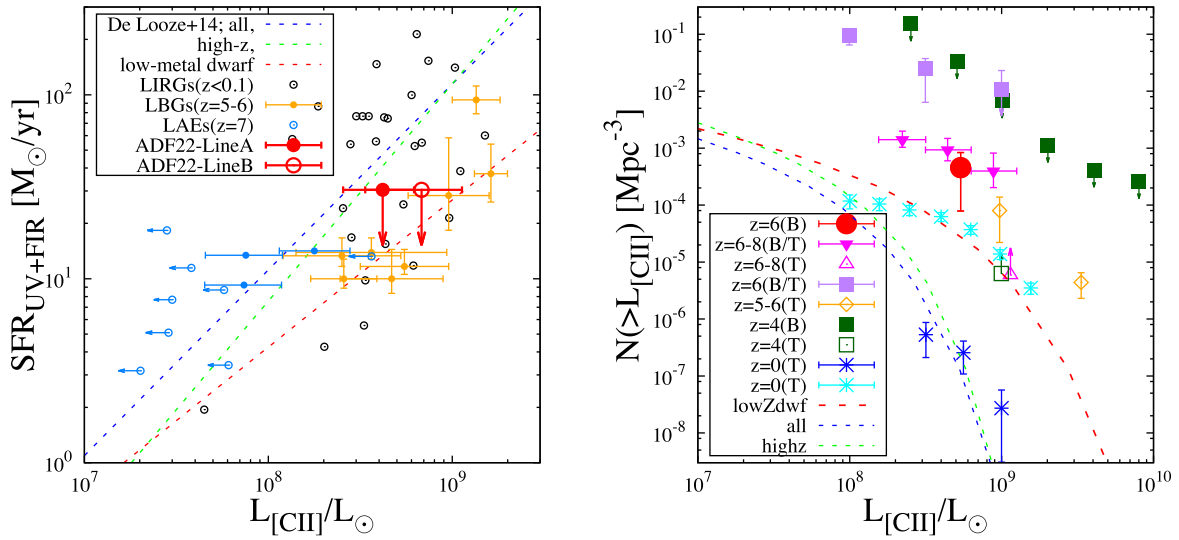

Fig. 9. Left: We compare the [C II] emitter candidates with other LIRGs (Maiolino et al. 2009), LBGs at $z = 5.2$–5.7 (Capak et al. 2015), and LAEs at $z = 6.6$–7.2 (Pentericci et al. 2016) in the SFR–$L_{[C\,II]}$ plane. The dashed lines represent empirical SFR–$L_{[C\,II]}$ relations given by De Looze et al. (2014) for different populations. The SFR–$L_{[C\,II]}$ relation for metal-poor dwarfs is consistent with the upper limit of SFR_{UV+FIR} of [C II] emitter candidates. Right: We summarize the redshift evolution of the [C II] luminosity function ([C II] LF) (Swinbank et al. 2012; Hemmati et al. 2017; Matsuda et al. 2015; Capak et al. 2015; Miller et al. 2016; Aravena et al. 2016b). The estimations from targeted observations are denoted by (T), and blind surveys are denoted by (B). We estimate [C II] LF at $z = 6.2$ from blind detection on the assumption that one of the two unconfirmed lines is a [C II] line at $z \sim 6$. The error-bar on our point uses Gehrels (1986). We also plot model of [C II] LFs at $z = 6$ calibrated by using the SFR function at $z = 6$ (Smit et al. 2012) and the SFR–$L_{[C\,II]}$ relation by De Looze et al. (2014). The observational results at $z > 4$ show good agreement with the predicted LF for metal-poor dwarfs. (Color online)

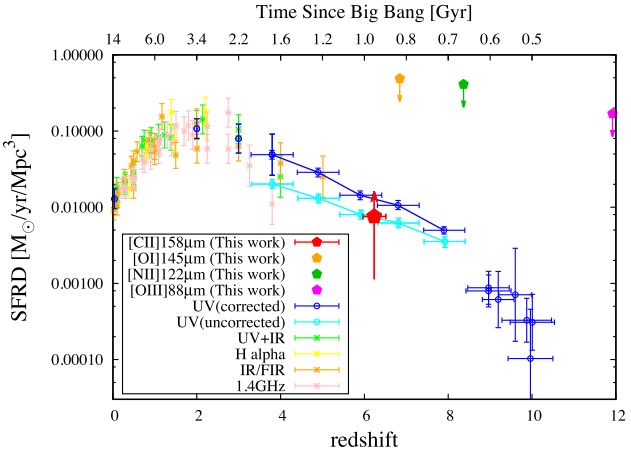

Fig. 10. Cosmic SFRD as a function of redshift. We show lower limit of a [C II] SFRD at $z = 6$ derived from the mean SFR of the two [C II] candidates divided by the survey volume. We also estimate the upper limits for the undetected fine-structure lines at $z = 7$–12. We plot the SFRD estimated by rest-frame UV observations (Oesch et al. 2014; Capak et al. 2015) and other wave bands (Behroozi et al. 2013). The estimation of [C II] SFRD from a conservatively selected source is already consistent with the dust-uncorrected UV SFRD at $z = 6$. (Color online)

$z = 6.0$ and 6.5 with $>6\sigma$. [C II] emitter candidates are faint in all counterparts. The line species of the CO emitters are identified by SED fitting or follow-up spectral observations. For [C II] emitter candidates, the possibility of other line emissions are excluded by discussion about number counts, line ratio, and EWs. Since one spurious source is possibly contaminated with the candidates, we assume at least one of the two candidates to be a real [C II] emitter. We constrain the $z = 6$ [C II] LF for one source and found that the [C II] LFs at $z > 4$ show good agreement with the predicted LF by using the SFR–$L_{[C\,II]}$ relation calibrated by local metal-poor dwarfs. We also found that estimated [C II]-based SFRs are consistent with the upper limit of the total SFR if we use the SFR–$L_{[C\,II]}$ relation for local metal-poor dwarfs. We estimate a conservative limit of [C II] SFRD at $z = 6.2$ for one source, which is close to the dust-uncorrected UV SFRD at $z = 6.2$. The results might imply that a mm/submm line survey is a powerful probe to estimate untraceable SFRD components from rest-UV observation at high redshift. The constraint for a faint-end slope of the [C II] LF from further line surveys and FIR/UV follow-up observations will give us the truth of such an implication and a detailed picture of cosmic star-formation history.

Acknowledgement

This work was supported by the ALMA Japan Research Grant of National Astronomical Observatory of Japan (NAOJ) Chile Observatory, NAOJ-ALMA-0071 and NAOJ-ALMA-0160. NHH was supported by the grant of NAOJ Visiting Fellow Program supported by the Research Coordination Committee, National Astronomical Observatory of Japan (NAOJ) and by funding from Foundation for

Promotion of Astronomy. IRS acknowledges support from STFC (ST/L00075X/1), the ERC Advanced Grant DUSTYGAL (321334) and a Royal Society Wolfson Research Merit Award.

This paper makes use of the following ALMA data: ADS/JAO.ALMA#2013.1.00162.S. ALMA is a partnership of ESO (representing its member states), NSF (USA) and NINS (Japan), together with NRC (Canada) and NSC and ASIAA (Taiwan) and KASI (Republic of Korea), in cooperation with the Republic of Chile. The Joint ALMA Observatory is operated by ESO, AUI/NRAO, and NAOJ. Data analysis was carried out on a common-use data analysis computer system at the Astronomy Data Centre (ADC) of the NAOJ. IRAC data was reduced and provided by J. Huang. The authors wish to thank A. Sternberg, E. Seaquist, L. Yao, M. Oguri, H. Nagai, I. Shimizu, and K. Mawatari. Finally, we are grateful to the referee for their useful comments and suggestions.

References

Aravena, M., et al. 2016a, ApJ, 833, 68
Aravena, M., et al. 2016b, ApJ, 833, 71
Asano, R. S., Takeuchi, T. T., Hirashita, H., & Nozawa, T. 2014, MNRAS, 440, 134
Barger, A. J., Wang, W.-H., Cowie, L. L., Owen, F. N., Chen, C.-C., & Williams, J. P. 2012, ApJ, 761, 89
Behroozi, P. S., Wechsler, R. H., & Conroy, C. 2013, ApJ, 770, 57
Blain, A. W., Smail, I., Ivison, R. J., & Kneib, J.-P. 1999, MNRAS, 302, 632
Blain, A. W., Smail, I., Ivison, R. J., Kneib, J.-P., & Frayer, D. T. 2002, Phys. Rep., 369, 111
Bolzonella, M., Miralles, J.-M., & Pelló, R. 2000, A&A, 363, 476
Bouwens, R. J., et al. 2012, ApJ, 754, 83
Bouwens, R. J., et al. 2016, ApJ, 833, 72
Brauher, J. R., Dale, D. A., & Helou, G. 2008, ApJS, 178, 280
Bruzual A., G., & Charlot, S. 1993, ApJ, 405, 538
Buat, V., et al. 2010, MNRAS, 409, L1
Burgarella, D., et al. 2013, A&A, 554, A70
Calzetti, D., Armus, L., Bohlin, R. C., Kinney, A. L., Koornneef, J., & Storchi-Bergmann, T. 2000, ApJ, 533, 682
Capak, P. L., et al. 2015, Nature, 522, 455
Carilli, C. L., & Walter, F. 2013, ARA&A, 51, 105
Carniani, S., et al. 2015, A&A, 584, A78
Carniani, S., et al. 2017, A&A, submitted (arXiv:1701.03468)
Casey, C. M., Narayanan, D., & Cooray, A. 2014, Phys. Rep., 541, 45
Chabrier, G. 2003, PASP, 115, 763
Chary, R., & Elbaz, D. 2001, ApJ, 556, 562
Chen, C.-C., et al. 2016, ApJ, 831, 91
Colbert, J. W., et al. 1999, ApJ, 511, 721
da Cunha, E., et al. 2013, ApJ, 765, 9
De Looze, I., et al. 2014, A&A, 568, A62
De Looze, I., Baes, M., Bendo, G. J., Cortese, L., & Fritz, J. 2011, MNRAS, 416, 2712
Decarli, R., et al. 2016a, ApJ, 833, 69
Decarli, R., et al. 2016b, ApJ, 833, 70
Díaz-Santos, T., et al. 2013, ApJ, 774, 68
Díaz-Santos, T., et al. 2016, ApJ, 816, L6
Dunlop, J. S., et al. 2017, MNRAS, 466, 861
Farrah, D., et al. 2013, ApJ, 776, 38
Fujimoto, S., Ouchi, M., Ono, Y., Shibuya, T., Ishigaki, M., Nagai, H., & Momose, R. 2016, ApJS, 222, 1
Geach, J. E., & Papadopoulos, P. P. 2012, ApJ, 757, 156
Gehrels, N. 1986, ApJ, 303, 336
Graciá-Carpio, J., et al. 2011, ApJ, 728, L7
Gruppioni, C., et al. 2013, MNRAS, 432, 23
Hainline, L. J., Blain, A. W., Smail, I., Frayer, D. T., Chapman, S. C., Ivison, R. J., & Alexander, D. M. 2009, ApJ, 699, 1610
Hatsukade, B., et al. 2016, PASJ, 68, 36
Hayashino, T., et al. 2004, AJ, 128, 2073
Hemmati, S., Yan, L., Diaz-Santos, T., Armus, L., Capak, P., Faisst, A., & Masters, D. 2017, ApJ, 834, 36
Herrera-Camus, R., et al. 2016, ApJ, 826, 175
Hollenbach, D., & McKee, C. F. 1989, ApJ, 342, 306
Inoue, A. K. 2003, PASJ, 55, 901
Inoue, A. K., et al. 2016, Sci, 352, 1559
Inoue, A. K., Shimizu, I., Tamura, Y., Matsuo, H., Okamoto, T., & Yoshida, N. 2014, ApJ, 780, L18
Iono, D., et al. 2006, ApJ, 645, L97
Kapala, M. J., et al. 2015, ApJ, 798, 24
Kaufman, M. J., Wolfire, M. G., Hollenbach, D. J., & Luhman, M. L. 1999, ApJ, 527, 795
Kennicutt, R. C., Jr. 1998, ApJ, 498, 541
Kousai, K, 2011, PhD thesis, Tohoku University
Kroupa, P. 2001, MNRAS, 322, 231
Kubo, M., et al. 2013, ApJ, 778, 170
Kubo, M., Yamada, T., Ichikawa, T., Kajisawa, M., Matsuda, Y., & Tanaka, I. 2015, ApJ, 799, 38
Lagos, C. d. P., Bayet, E., Baugh, C. M., Lacey, C. G., Bell, T. A., Fanidakis, N., & Geach, J. E. 2012, MNRAS, 426, 2142
Lehmer, B. D., et al. 2009, ApJ, 691, 687
McMullin, J. P., Waters, B., Schiebel, D., Young, W., & Golap, K. 2007, ASP Conf. Ser., 376, 127
Madau, P., & Dickinson, M. 2014, ARA&A, 52, 415
Maiolino, R., et al. 2005, A&A, 440, L51
Maiolino, R., et al. 2015, MNRAS, 452, 54
Maiolino, R., Caselli, P., Nagao, T., Walmsley, M., De Breuck, C., & Meneghetti, M. 2009, A&A, 500, L1
Matsuda, Y., Nagao, T., Iono, D., Hatsukade, B., Kohno, K., Tamura, Y., Yamaguchi, Y., & Shimizu, I. 2015, MNRAS, 451, 1141
Matsuda, Y., et al. 2004, AJ, 128, 569
Miller, T. B., Chapman, S. C., Hayward, C. C., Behroozi, P. S., Bradford, C. M., Willott, C. J., & Wagg, J. 2016, MNRAS, submitted (arXiv:1611.08552)
Nakamura, E., Inoue, A. K., Hayashino, T., Horie, M., Kousai, K., Fujii, T., & Matsuda, Y. 2011, MNRAS, 412, 2579
Oesch, P. A., et al. 2014, ApJ, 786, 108
Omont, A., et al. 2013, A&A, 551, A115
Ono, Y., Ouchi, M., Kurono, Y., & Momose, R. 2014, ApJ, 795, 5
Orsi, Á., Padilla, N., Groves, B., Cora, S., Tecce, T., Gargiulo, I., & Ruiz, A. 2014, MNRAS, 443, 799
Pentericci, L., et al. 2016, ApJ, 829, L11
Polletta, M., et al. 2007, ApJ, 663, 81
Popping, G., van Kampen, E., Decarli, R., Spaans, M., Somerville, R. S., & Trager, S. C. 2016, MNRAS, 461, 93
Rangwala, N., et al. 2011, ApJ, 743, 94
Salpeter, E. E. 1955, ApJ, 121, 161

Sargsyan, L., et al. 2012, ApJ, 755, 171
Simpson, J. M., et al. 2014, ApJ, 788, 125
Smail, I., Swinbank A. M., Ivison R. J., & Ibar E. 2011, MNRAS, 414, L95
Smit, R., Bouwens, R. J., Franx, M., Illingworth, G. D., Labbé, I., Oesch, P. A., & van Dokkum, P. G. 2012, ApJ, 756, 14
Suzuki, R., et al. 2008, PASJ, 60, 1347
Swinbank, A. M., et al. 2012, MNRAS, 427, 1066
Swinbank, A. M., et al. 2014, MNRAS, 438, 1267
Takeuchi, T. T., Buat, V., & Burgarella, D. 2005, A&A, 440, L17
Takeuchi, T. T., Hirashita, H., Ishii, T. T., Hunt, L. K., & Ferrara, A. 2003, MNRAS, 343, 839
Takeuchi, T. T., Ishii, T. T., Nozawa, T., Kozasa, T., & Hirashita, H. 2005, MNRAS, 362, 592
Tamura, Y., Saito, T., Tsuru, T. G., Uchida, H., Iono, D., Yun, M. S., Espada, D., & Kawabe, R. 2014, ApJ, 781, L39
Uchimoto, Y. K., et al. 2012, ApJ, 750, 116
Umehata, H., et al. 2017, ApJ, 835, 98
Vallini, L., Gruppioni, C., Pozzi, F., Vignali, C., & Zamorani, G. 2016, MNRAS, 456, L40
Venemans, B. P., et al. 2012, ApJ, 751, L25
Webb, T. M. A., Yamada, T., Huang, J.-S., Ashby, M. L. N., Matsuda, Y., Egami, E., Gonzalez, M., & Hayashimo, T. 2009, ApJ, 692, 1561
Williams, J. P., de Geus, E. J., & Blitz, L. 1994, ApJ, 428, 693
Willott, C. J., Carilli, C. L., Wagg, J., & Wang, R. 2015, ApJ, 807, 180
Willott, C. J., Omont, A., & Bergeron, J. 2013, ApJ, 770, 13
Wolfire, M. G., Hollenbach, D., & McKee, C. F. 2010, ApJ, 716, 1191
Wolfire, M. G., Hollenbach, D., McKee, C. F., Tielens, A. G. G. M., & Bakes, E. L. O. 1995, ApJ, 443, 152
Zhou, L., Shi, Y., Diaz-Santos, T., Armus, L., Helou, G., Stierwalt, S., & Li, A. 2016, MNRAS, 458, 772